

A particular carbon-chain-producing region: L1489 starless core

Yuefang Wu¹, Lianghao Lin^{1,2,3}, Xunchuan Liu¹, Xi Chen^{4,5}, Tie Liu^{6,7}, Chao Zhang^{1,8}, Binggang Ju³, Jinghua Yuan⁹, Junzhi Wang⁴, Zhiqiang Shen⁴, Kee-Tae Kim⁶, Sheng-Li Qin⁸, Juan Li⁴, Hongli Liu¹⁰, Tianwei Zhang¹, Ye Xu³, and Qinghui Liu⁴

¹ Department of Astronomy, Peking University, 100871, Beijing, China
e-mail: ywu@pku.edu.cn

² School of Astronomy and Space Sciences, University of Science and Technology of China, 96 Jinzhai Road, Hefei, 230026, China

³ Purple Mountain Observatory and Key Laboratory of Radio Astronomy, Chinese Academy of Sciences, 8 Yuanhua Road, Nanjing, 210034, China

⁴ Shanghai Astronomical Observatory, Chinese Academy of Sciences, Shanghai 200030, China

⁵ Center for Astrophysics, Guangzhou University, Guangzhou, 510006, China

⁶ Korea Astronomy and Space Science Institute, 776 Daedeokdae-ro, Yuseong-gu, Daejeon 34055, Korea

⁷ East Asian Observatory, 660 North A'ohoku Place, Hilo, HI 96720, USA;

⁸ Department of Astronomy, Yunnan University, Kunming, 650091, China

⁹ National Astronomical Observatories, Chinese Academy of Sciences, 20A Datun Road, Chaoyang District, Beijing 100101, China

¹⁰ Department of Physics, The Chinese University of Hong Kong, Shatin, NT, Hong Kong SAR

March 17, 2022

ABSTRACT

We detected carbon-chain molecules (CCMs) HC_{2n+1}N ($n=1-3$) and C_3S in K_u band as well as high-energy excitation lines including C_4H $\text{N}=9-8$, $\text{J}=17/2-15/2$, $19/2-17/2$, and CH_3CCH $\text{J}=5-4$, $\text{K}=2$ in the 3 mm band toward a starless core called the eastern molecular core (EMC) of L1489 IRS. Maps of all the observed lines were also obtained. Comparisons with a number of early starless cores and WCCC source L1527 show that the column densities of C_4H and CH_3CCH are close to those of L1527, and the CH_3CCH column densities of the EMC and L1527 are slightly higher than those of TMC-1. The EMC and L1527 have similar C_3S column densities, but they are much lower than those of all the starless cores, with only 6.5% and 10% of the TMC-1 value, respectively. The emissions of the N-bearing species of the EMC and L1527 are at the medium level of the starless cores. These comparisons show that the CCM emissions in the EMC are similar to those of L1527, though L1527 contains a protostar. Although dark and quiescent, the EMC is warmer and at a later evolutionary stage than classical carbon-chain-producing regions in the cold, dark, quiescent early phase. The PACS, SPIRE, and SCUBA maps evidently show that the L1489 IRS seems to be the heating source of the EMC. Although it is located at the margins of the EMC, its bolometric luminosity and bolometric temperature are relatively high. Above all, the EMC is a rather particular carbon-chain-producing region and is quite significant for CCM science.

Key words. ISM: molecules — ISM: abundances — stars: formation — ISM: individual object (L1489)

1. Introduction

Carbon-chain molecules (CCMs), including radicals, have the largest number of atoms among interstellar molecules found up until now¹. They have a large mass range and have different excitation energies and active states, and as a result they play important roles in interstellar chemical and physical processes. Although it is difficult for them to exist in terrestrial conditions, they were detected in star-forming regions and circumstellar envelopes of evolved stars (Turner 1971; Avery et al. 1976; Suzuki et al. 1992; Taniguchi et al. 2018; Winnewisser & Walmsley 1978; Ziurys 2006; Zhang et al. 2017).

In molecular clouds, CCMs were found to be abundant in dark and quiescent cores. TMC-1 is the typical carbon-chain-producing region. Molecules of HC_7N , HC_9N , and HC_{11}N were first detected in this core (Kroto et al. 1978; Broten et al. 1978; Bell et al. 1997). Almost all CCMs found so far, including C_nO and C_nS , were discovered in TMC-1 (Herbst et al. 1984;

Matthews et al. 1984; Irvine et al. 1988). High-resolution maps of a number of S-bearing and N-bearing species were made and at least six cores were detected in the TMC-1 ridge (Hirahara et al. 1992). Changes in molecular abundances along the ridge were analyzed with the dynamical-chemical model (Markwick et al. 2000). In addition to TMC-1, L1521B, L1498, L1544, and L1521E were also detected as rich starless carbon-chain-producing regions (Suzuki et al. 1992; Kuiper et al. 1996; Ohashi et al. 1999; Hirota et al. 2002). All these cores in the molecular complex Taurus are in an early stage of CCM chemistry. Meanwhile a number of starless cores outside of Taurus, such as L492, Lupus-1A, L1512, and Serpens South 1a (Serp S1a), have been found to be abundant carbon-chain-producing regions (Hirota & Yamamoto 2006; Sakai et al. 2010b; Cordiner et al. 2011; Friesen et al. 2013; Li et al. 2016). Starless and dark cores CB 130-3 in the Aquila rift region and L673-SMM4 in Cloud B of L673 were also identified as carbon-chain-producing regions (Hirota et al. 2011). Recently, 17 high-mass starless cores (HMSCs) and 35 high-mass protostellar objects (HMPOs) were

¹ www.astro.uni-koeln.de/cdms/molecules

surveyed with HC_3N and HC_5N by Taniguchi et al. (2018). The molecule HC_3N was detected in 15 HMSCs and 28 HMPOs, and HC_5N was found in 5 HMSCs and 14 HMPOs (Taniguchi et al. 2018).

All these cores are in an early chemical phase. However, their properties and evolutionary states could be somewhat different. In L1498, radial chemical differentiation has been detected with C_2S and NH_3 distributed in an onion shell-like structure with NH_3 at the inner part and C_2S at the outer part, which may have resulted from a slowly contracting dense core with a growing outer envelope (Kuiper et al. 1996). A similar structure of C_2S emission was discovered in L1544, which was interpreted as a result of infall and rotation by Ohashi et al. (1999). Their different evolutionary states can be sensitively traced with abundance ratios of CCMs and NH_3 (Olano et al. 1988; Suzuki et al. 1992; Hirota & Yamamoto 2006).

In star-forming cores, CCMs are usually less abundant than in early cold and dark cores (Sakai et al. 2008). In particular, the abundance of S-bearing species is significantly lower in protostellar cores (Suzuki et al. 1992).

However, in 2008 the protostellar core L1527 containing an infrared source IRAS 04368+2557 was found as a CCM-harboring region (Sakai et al. 2008). High-energy excitation lines (upper level energy $E_{up} > 20$ K; Sakai et al. 2008) of carbon-chain molecules such as C_4H_2 ($10_{0,10} - 9_{0,9}$), $\text{C}_4\text{H } N = 9 - 8$, $l\text{-C}_3\text{H}_2$ ($4_{1,3} - 3_{1,2}$), and $\text{CH}_3\text{CCH } J = 5 - 4$, $K = 2$ were detected in this source. The intensity (T_{MB}) of the line $\text{C}_4\text{H } N = 9 - 8$, $J = 19/2 - 17/2$ reaches 1.7 K. These results are unusual since CCMs are generally absent in star-forming regions. A hypothesis was proposed to explain these findings. Since the evaporation temperature of CH_4 is about 30 K, it can be abundant in some warmer regions around protostellar objects (Sakai et al. 2009). Subsequently, CH_4 reacts with C^+ to form hydrocarbon ions. Such processes were proposed as warm carbon-chain chemistry (WCCC) by Sakai et al. (2008), which is different from the chemistry in early cores. More recently, formation of CCMs in WCCC (lukewarm corinos) was modeled with the macroscopic Monte Carlo method and it was found that the amount of CH_4 can diffuse inside the ice mantle, and therefore sublimation upon warm-up plays a crucial role in the synthesis of carbon-chain species in the gas phase (Wang et al. 2019).

A second WCCC source, IRAS 15398-3359, was found by Sakai et al. (2009) very shortly after the discovery of L1527. A massive star-forming region NGC 3576 was also revealed as a WCCC source according to the detected $\text{C}_5\text{H } J = 39/2 - 37/2$ (Saul et al. 2015).

In addition to high-energy excitation lines of hydrocarbons, other kinds of CCM emission lines exist in WCCC sources. N-bearing CCMs have been detected in all the WCCC sources found so far. Spectral lines of HC_3N , HC_5N , HC_7N , and even HC_9N have been seen in L1527. Furthermore, $\text{HC}_3\text{N } J = 10 - 9$ and $\text{HC}_5\text{N } J = 32 - 31$, the latter being a very-high-energy excitation transition, were detected in the second WCCC source (Sakai et al. 2008, 2009; Saul et al. 2015; Benedettini et al. 2012). $\text{HC}_3\text{N } J = 11 - 10$ was detected in NGC 3576 (Saul et al. 2015).

L1489 is a famous low-mass star-forming source located in Taurus with a distance of 140 PC (Myers et al. 1988). In this paper we report CCM emissions detected towards the L1489 starless core, that is, the eastern molecular core (EMC) of the L1489 IRS (Benson & Myers 1989; Caselli et al. 2002). We made observations of multiple spectral lines of CCMs for this core, including emissions of N- and S-bearing CCMs in the K_u band and high-energy excitation transitions in the 3 mm band.

The observations are described in the following section. In Sect. 3 we present the results. The discussions are presented in Section 4 and a summary is given in Sect. 5.

2. Observation

First we observed the spectral lines toward R.A.(J2000)=04:04:47.5, Dec.(J2000)=26:19:42, which is the center of the high-visual-opacity region (Benson & Myers 1989) of L1489 (hereafter O point, which is also taken as the coordinate reference position in this work). We then mapped this source.

The lines we observed include the transitions of N-bearing and S-bearing species $\text{HC}_3\text{N } J = 2 - 1$, $\text{HC}_5\text{N } J = 6 - 5$, $\text{HC}_7\text{N } J = 14 - 13$, $J = 15 - 14$, $J = 16 - 15$ as well as $\text{C}_3\text{S } J = 3 - 2$ in K_u band, and $\text{C}_4\text{H } N = 9 - 8$, $J = 19/2 - 17/2$, $J = 17/2 - 15/2$, $\text{CH}_3\text{CCH } J = 5 - 4$, $K=0$, $J = 5 - 4$ $K=1$, and $J = 5 - 4$, $K=2$, $c\text{-C}_3\text{H}_2$ ($2_{1,2} - 1_{0,1}$) as well as $\text{HC}_3\text{N } J = 10 - 9$ in the 3 mm band. The parameters of the observed transitions listed in Table 1 are quoted from the molecular database at “Splat-alogue”² that is a compilation of the Jet Propulsion Laboratory (Pickett et al. 1998), Cologne Database for Molecular Spectroscopy (CDMS; Müller et al. 2005), and Lovas/NIST (Lovas 2004) catalogs. This source was searched for $\text{HC}_3\text{N } J = 4 - 3$, $J = 5 - 4$, $\text{HC}_5\text{N } J = 8 - 7$, $J = 17 - 16$ as well as $\text{C}_2\text{S } J_N = 2_1 - 1_0$, $J_N = 4_3 - 3_2$ (Suzuki et al. 1992; Fuller & Myers 1993; Brinch et al. 2007). All the transitions in this work were observed for the first time.

2.1. Observed with TMRT 65 m telescope

The spectral lines at K_u band were observed with the Tian Ma Radio Telescope (TMRT) of Shanghai Observatory on Jan 25, 2016, and Dec 2-4, 2017. The TMRT is a newly built 65 m diameter fully steerable radio telescope located in the western suburb of Shanghai (Li et al. 2016). The front end of the K_u band is a cryogenically cooled receiver covering the frequency range of 11.5–18.5 GHz. The pointing accuracy is better than $10''$. An FPGA-based spectrometer based upon the design of Versatile GBT Astronomical Spectrometer (VEGAS) was employed as the Digital backend system (DIBAS) (Bussa & VEGAS Development Team 2012). For molecular line observations, DIBAS supports a variety of observing modes, including 19 single sub-band modes and 10 modes with eight sub-bands each. The center frequency of the sub-band is tunable to an accuracy of 10 kHz. For our observation, the DIBAS mode 22 was adopted. Each of the eight side-bands has a bandwidth of 23.4 MHz and 16384 channels. The main beam efficiency is 60% at the K_u band (Wang et al. 2015; Li et al. 2016). The beam sizes and the equivalent velocity resolutions are given in the last two columns of Table 1, respectively. After the spectra at O point were observed, we made nine-point mapping observations on Dec 2-3, 2017. The observations were performed in point-by-point mode around a point 1' south of the O point to cover the L1489 IRS. We start the map in a square pattern and with a grid separation of 1'; its diagonal lines are along E-W and N-S directions. To cover the northern part of the emission region, we added four sampling points: (1,0), (0,0.5), (0,-0.5), and (-0.5,0) on Dec 4, 2017.

² www.splatologue.net

2.2. Observed with the Purple Mountain Observatory telescope

The spectral lines at 3 mm were observed with the 13.7 m telescope of the Qinghai Station of the Purple Mountain Observatory (PMO) on March 31, 2017. The pointing and tracking accuracies were both better than 5". The main beam efficiency is 59%³. A Superconducting Spectroscopic Array Receiver with sideband separation was employed at the front end (Shan et al. 2012) while at the back end a Fast Fourier Transform Spectrometer with a total bandwidth of 1 GHz allocated to 16,384 channels was used. The observed lines were covered in the two sidebands with frequencies from 85 to 86 GHz and 90 to 91 GHz, respectively. The spectral resolution is about 61 kHz. The system temperatures are in the range of 139–149 K, with a mean value of 144 K. The position-switch mode was adopted. The on-source time was about 25 minutes for all observed lines except CH₃CCH $J=5-4$ which took an integrating time of about 20 hours and was completed on Dec 10-14, 2018. The maps were carried out with the on-the-fly mode on Nov 1, 2017. The mapping region is 15'×15' for the lines of the CCMs in the 3 mm band with a 20''×20'' grid.

The IRAM software package GILDAS including CLASS and GREG was used for all the line data reduction (Guilloteau & Lucas 2000).

3. Results

All the transitions in K_u band and 3 mm band are detected towards the EMC. Hyperfine lines of HC₃N $J = 2 - 1$ and HC₅N $J = 6 - 5$ are detected. The velocity separation between $F = 7 - 6$ and $F = 6 - 5$ of HC₅N $J = 6 - 5$ is ~0.3 km/s. Kaifu et al. (2004) detected HC₅N $J = 6 - 5$ in TMC-1 with the Nobeyama 45 m radio telescope. The hyperfine structures were not resolved at that time due to their slightly poorer spectral resolution (~0.7 km/s). Li et al. (2016) detected this line towards Serpens South 1a with TMRT 65 m. However, only the HC₅N $J = 6 - 5$, $F = 5 - 4$ was resolved because the line width of Serpens South 1a is about 0.5 km/s. Three hyperfine components $F = 7 - 6$, $F = 6 - 5$, and $F = 5 - 4$ of HC₅N $J = 6 - 5$ are fully resolved for the first time.

3.1. Emissions of HC₃N $J = 2 - 1$

Panel (a) of Figure 1 presents the HC₃N $J = 2 - 1$ spectrum and its wing at the peak position of the HC₃N map. In total, five hyperfine lines of HC₃N $J = 2 - 1$ are well resolved, with the strongest one labeled as $J = 2 - 1$, $F = 3 - 2$ with a T_{MB} as high as 3.23 K. When zooming in on the hyperfine component HC₃N $J = 2 - 1$, $F = 3 - 2$ shown in panel (b), it is clear to see that the residual spectrum after removing the Gaussian component displays a red wing. The velocity of the shifted gas has a width of 0.33 km s⁻¹ spanning from 6.75 to 7.08 km s⁻¹. Panel (c) shows the contours of the integrated intensity of the red wing with a maximum value of 0.14 K km s⁻¹ and a σ of 0.02 K km s⁻¹ overlaid on the map of the integration of line center. The red wing may belong to high-velocity gas since the profile of the wing is rather smooth and the ratio of the wing range to the FWHM of the line is similar to that of the red wing of the molecular outflow S140 (Lada 1985). However, foreground and background cold gas as well as additional components cannot be excluded (Wu et al. 2005). High-resolution observations may be

useful to identify its origin. Further discussions are excluded in the following analysis.

3.2. Spectral lines and emission regions

The spectral lines of HC₅N $J = 6 - 5$ and HC₇N $J = 14 - 13$, $J = 15 - 14$, $J = 16 - 15$ as well as the C₃S $J = 3 - 2$ at the map peak position (P point, see below) are shown in the left panel of Fig. 2; the spectrums of HC₃N $J = 2 - 1$, $F = 3 - 2$ are presented in Fig. 1(a). The spectral lines of c-C₃H₂ (2_{1,2}-1_{0,1}), CH₃CCH $J = 5(0) - 4(0)$, and HC₃N $J = 10 - 9$ in the 3 mm band at the P position (see below) are presented in the left panel of Fig. 3. The K=0, 1, and 2 of CH₃CCH $J = 5 - 4$ were all detected using PMO with a long integration time and are presented in the left panel of Fig. 5. The signal-to-noise ratio (S/N) of the weakest K=2 hyperfine line is larger than 5.

All the spectral lines were fitted with a Gaussian function. The line parameters including the central velocity V_{LSR} , the main beam temperature T_{MB} , the full width at half maximum (FWHM), and integrated intensities are listed in columns 3-5 of Table 2. One can see that all the lines have a V_{LSR} of about 6.6 km s⁻¹ except for C₄H and c-C₃H₂ whose V_{LSR} are about (6.8-6.9) km s⁻¹. The FWHMs of these two lines (C₄H and c-C₃H₂) are also broader than those of other detected CCM lines.

Integrated intensity maps of all the detected lines were made. The maps of the lines in K_u and the 3 mm band are presented in the right panels of Figs. 2 and 3, respectively.

One can see from the right-hand panels of Figs. 2 and 3 that the emission peaks (black hollow triangle) of transitions of N-bearing species in K_u band are relatively consistent with each other. This peak point (P point hereafter) is located at R.A.(J2000)= 04:04:47.5, Dec.(J2000)=26:19:12, about 0.5 arcmin south of the O point (black square) and 1 arcmin east of the IRS (hexagonal star). The emission peaks of other lines are all with some deviations from the P point. For example, the peak of c-C₃H₂ (green filled hollow triangle in Fig. 3) is located at < 0.5 arcmin south of the P point. These deviations are due to different chemical and dynamical properties of different molecular species and can often be seen in molecular cores such as the NH₃ cores in Orion, Cepheus, and H₂O maser sources as well as various gas cores in the carbon-chain-producing region NGC 3576 (Harju et al. 1993; Wu et al. 2006; Saul et al. 2015, see also Fig. 7 and Sect. 4.1). We take the P point as the peak of the emissions of all the CCMs except C₃S $J = 3 - 2$.

3.3. Lines at O point

Single point observations towards O point were made before the map. The highest S/Ns of the data at this point were compared to those of other points. The comparison enabled us to analyze the profile of molecular lines in detail. The lines at O point are thus also shown in Fig. 4. The left panel of Fig. 4 presents the spectral lines of HC₃N, HC₅N, HC₇N, and C₃S in the K_u band. The right panel presents the spectral lines of C₄H, CH₃CCH, c-C₃H₂, and HC₃N in 3 mm band.

The spectral peak of the HC₇N $J = 14 - 13$ at O point shown in Fig. 4 seems to have a dip at the center with an S/N ≈ 3. The spectrum of HC₇N $J = 15 - 14$ may also be split but interference of noise cannot be excluded. This was not seen in the spectrums of other CCMs in the K_u or 3 mm bands at O point. For the emission of C₃S $J = 3 - 2$, the T_{MB} at O point is higher than that at P point, and therefore O point is adopted as the peak of the C₃S core.

³ <http://www.radioast.nsd.cn/zhuangtaibaogao.php>

3.4. Column density

The column densities of the observed CCMs except C₃S were calculated from the integrated intensities of lines of P point. For C₃S, parameters at O point are adopted. Assuming the gas is in local thermodynamic equilibrium (LTE) and the lines are optically thin, the column densities are calculated with the solution of the radiation transfer equation (Garden et al. 1991; Mangum & Shirley 2015)

$$N = \frac{3k}{8\pi^3\nu} \frac{Q}{\sum S_{ij}\mu^2} \exp\left(\frac{E_{up}}{kT_{ex}}\right) J(T_{ex}) \int \tau dV, \quad (1)$$

$$T_{MB}/\eta = f \frac{h\nu}{k} [(e^{\frac{h\nu}{kT_{ex}}} - 1)^{-1} - (e^{\frac{h\nu}{kT_{bg}}} - 1)^{-1}] [1 - e^{-\tau}], \quad (2)$$

where S_{ij} , μ , and Q are the line strength, the permanent dipole moment, and the partial function, respectively, which are quoted from “Splatalogue”, and T_{MB} is the main beam temperature, η is the efficiency of the main beam, and f is the beam filling factor, assumed to be unity.

The excitation temperature was calculated using different methods in this work for comparison. Using the hyperfine structure (HFS) fitting program in GILDAS/CLASS, we performed hyperfine structure fitting toward spectra of HC₃N $J = 2 - 1$. The optical depth of the main component was obtained as $\tau = 0.45 \pm 0.12$ and an excitation temperature of 11.5 ± 1.0 K was derived through Eq. 2 with $T_{bg} = 2.73$ K and a beam filling factor of unity. We use the lines $K=0, 1$, and 2 of CH₃CCH $J = 5 - 4$ to derive the rotational temperature T_{rot} and a value of 12.6 ± 1.0 K was obtained (see the middle panel of Fig. 5). Since the $K=1, 2$ levels of CH₃CCH $J=5-4$ are easily thermalized and even more easily than NH₃ (1,1) (2,2), the kinetic temperature T_k is assumed equal to T_{rot} , 12.6 ± 1.0 K (Askne et al. 1984; Evans 1980).

Continuum data from far-infrared to sub-millimeter are available for the L1489 region⁴. The dust temperature (T_d) and H₂ column density were derived via modeling the PACS and SPIRE data of Herschel at 160, 250, 350, and 500 μ m (see Table 3 and the right panel of Fig. 5) to a modified black body:

$$S_\nu = B_\nu(T)(1 - e^{-\tau_\nu})\Omega, \quad (3)$$

where $\tau_\nu = \mu_{H_2} m_H \kappa_\nu N_{H_2} / R_{gd}$; here $\mu_{H_2} = 2.8$ is the mean molecular weight adopted from Kauffmann et al. (2008), m_H is the mass of a hydrogen atom, N_{H_2} is the column density, and $R_{gd} = 100$ is the ratio of gas to dust. The dust opacity κ_ν can be expressed as a power law of frequency,

$$\kappa_\nu = 5.9(\nu/850 \text{ GHz})^\beta \text{ cm}^2 \text{ g}^{-1}, \quad (4)$$

with $\kappa_\nu(850 \text{ GHz}) = 5.9 \text{ cm}^2 \text{ g}^{-1}$ adopted from Ossenkopf & Henning (1994). The free parameters are the dust temperature, dust emissivity index β , and column density. The fitting results give $T_d = 13.8 \pm 0.2$ K and $N_{H_2} = (1.02 \pm 0.07) \times 10^{22} \text{ cm}^{-2}$ with $\beta = 1.75$.

These derived temperatures are listed in Table 4. The T_d variation from the inner to outer parts of the core, which was model fitted from the SCUBA 850 μ m image (Ford & Shirley 2011), is also listed in Table 4. These values are comparable with the kinetic temperature of L1527 (12.3 ± 0.8 K) and that of IRAS 15398-3359 (12.6 K; Sakai et al. 2008, 2009). Therefore, a unified excitation temperature of 12.6 K was adopted for calculating column densities and for further analyses.

⁴ <http://www.cosmos.esa.int/web/herschel/science-archive>

For the column density of the detected species, only that of CH₃CCH can be derived by analysis of multiple transitions at different energy levels. For other species including the hyperfine lines of HC₅N and multiple rotation lines of HC₇N, the upper level energies of the multiple lines are close to one another and this method is impractical. The average values of column densities calculated from multiple lines weighted by T_{MB}/σ was therefore adopted as the species column density.

The T_{ex} uncertainty will bring in about 10% error for calculation of column densities of all the species.

The column densities are listed in Table 2. The uncertainties of column densities are derived from errors of T_{ex} and line integrated intensities. The column densities of our N-bearing molecules range from 1.4×10^{12} to $4.5 \times 10^{13} \text{ cm}^{-2}$. Among all the detected molecules in the K_u band, C₃S has the lowest column density, $0.8 \times 10^{12} \text{ cm}^{-2}$, which is much lower than those of starless cores such as TMC-1, L1544, and L1498 (Suzuki et al. 1992); this is also lower than that of the stellar core L1251A (Cordiner et al. 2011).

4. Discussion

4.1. Carbon-chain molecule emission characteristics

The species C₄H $N=9-8$, $J = 19/2-17/2$, $17/2-15/2$ and CH₃CCH $J=5-4$, $K=0, 1, 2$ were detected in the WCCC source L1527 (Sakai et al. 2008). CH₃CCH $J=5-4$, $K=2$ is the highest-excitation line detected in L1527. All of these lines were detected in the EMC. In the EMC, N-bearing species appear to be relatively abundant while C₃S is very weak.

Figure 6 presents the CCM column densities of the EMC and L1527 as well as the five early carbon-chain-producing regions normalized by the values of TMC-1. One can see that the column densities of the species with high-energy excitation lines in the EMC and L1527 are close to each other. The CH₃CCH column densities of the two cores are slightly higher than that of TMC-1 while their values of C₄H are lower than that of TMC-1. Among five starless cores, L1521B is the only one where the C₄H is detected. It is worth noting that the column density of C₄H in L1521B is even higher than that of TMC-1. In this source the detected C₄H line is $N = 2-1$ $J = 5/2-3/2$, $F = 2-1, 3-2$ with an upper level energy of 1.4 K, which is much lower than those of lines detected in the EMC and L1527 (Hirota et al. 2004). However, the HC₃N $J=10-9$ with E_{up} 24.0 K was detected in the starless core L1498 (Tafalla et al. 2006). Since only the EMC and L1498 have this transition observed, it was not plotted on Fig. 6.

From Fig. 6 one can also see that among all the starless cores, the column densities of the N-bearing species in the EMC and L1527 are at the intermediate level. The HC₃N column density in the EMC is higher than that of L1527. The N-bearing species seem to be abundant in WCCC sources in general. In the WCCC source IRAS 15398-3359, a very-high-energy excitation line of HC₅N $J=32-31$ with E_{up} 67.5 K was detected though the detection is tentative (Sakai et al. 2009). The HC₃N column density in IRAS 15398-3359 is $1.5 \times 10^{14} \text{ cm}^{-2}$ (Wu et al. in preparation). In the massive core WCCC source NGC 7536 the HC₅N column density is $1 \times 10^{13} \text{ cm}^{-2}$ which is derived from the detected line of HC₅N $J=11-10$ (Saul et al. 2015). The E_{up} of the HC₅N $J=11-10$ transition is 28.8 K.

As for the S-bearing species, Fig. 6 shows that the column density of the EMC is a little lower than that of L1527. However, C₃S column densities of both sources, about 6.5% (EMC) and 10% (L1527) of the TMC-1 value, respectively, are much lower

than all of the compared early starless cores. It was recognized previously that S-bearing species are usually deficient in star-forming cores. A number of low-mass star-forming cores were examined for emissions of S-bearing CCMs by Suzuki et al. (1992). Results showed no or marginal detection for most protostellar cores and L1489 was taken as an example. In the EMC, the emission of C_3S $J = 2 - 1$ at P point is also marginally detected. Our C_3S $J = 3 - 2$ map shows that the emission peak of C_3S $J = 3 - 2$ (O point) is separated from those of N-bearing species and NH_3 (Myers et al. 1988), similar to the cases of L1498 and L1544. But even at the O point, the column density of the C_3S is still much lower than those of L1544 and L1498.

All these comparisons present the following characteristics of the EMC.

1. Emissions of the species with high-energy excitation lines of the EMC are close to those of L1527. For these two sources the column densities of the species with high-energy excitation lines are comparable with those of TMC-1.

2. For the N-bearing species, the column densities of the EMC and L1527 are at the medium level among all the samples.

3. The column density of C_3S of the EMC is close to that of L1527 but is much lower than those of all starless cores.

In short, the CCM emissions of the EMC are similar to those of L1527 but deviate from the early cold starless cores.

4.2. Core status and environment

L1489 is one of the 90 small visually opaque regions chosen from the Palomar Sky Atlas prints (Myers et al. 1983). NH_3 (1,1) mapping presents a gas core which is about half an arcminute south of the high visual opacity and about one arcminute east of the IRAS 04016+2610, which was revealed as a Class I IRS (Myers et al. 1988, 1987). This region was also mapped with N_2H^+ $J=1-0$ (Caselli et al. 2002). The peak positions of the NH_3 (1,1) and N_2H^+ $J=1-0$ map are closely coincident with our P point (1 arcmin east of L1489 IRS). These observations confirm that the EMC is dark and starless, similar to those early starless cores presented in Fig. 6.

The C_2S distributions of L1498 and L1544 have a central hole which can be explained with infall and rotation (Hirota & Yamamoto 2006; Ohashi et al. 1999). In the EMC no sign of collapse or rotation has been detected so far and it is quiescent. At P point there is strong NH_3 emission together with weak C_3S emission, which may be related to the evolutionary state of the core (Suzuki et al. 1992; Hirota & Yamamoto 2006).

The abundance ratios of NH_3/C_2S of TMC-1, L1521B, L492, L1498 and L1544 range from 2.9 to 25 (Hirota & Yamamoto 2006). For the EMC, using the NH_3 column density of Myers et al. (1988) and the C_2S column density estimated from C_3S emission with an average abundance ratio C_2S/C_3S of 4.3 ± 0.9 derived from the data of starless cores including L1498, L1521B, TMC-1 and L1544 (Suzuki et al. 1992), the ratio of NH_3/C_2S is 289. This is one order of magnitude larger than the largest of the seven cores listed in Hirota & Yamamoto (2006). It is also larger than the NH_3/C_2S ratio of 37 for Serp S1a, which was derived from NH_3 and C_3S column densities with the ratio of C_2S/C_3S 4.3 (Friesen et al. 2013; Li et al. 2016; Suzuki et al. 1992). Serp S1a has a more active and complex environment than starless cores in Taurus and infall was detected (Friesen et al. 2013). These indicate that the EMC has the latest evolutionary state among all the starless cores shown in Fig. 6.

A prominent difference between the EMC and other early starless cores is the temperature and the thermalisation of the gas. In TMC-1 the rotational temperature ranges from 4 to 8 K

while the kinetic temperature ranges from 9 to 10 K (Kawaguchi et al. 1991; Kalenskii et al. 2004; Snyder et al. 2006; Sakai et al. 2008). The dust temperature is 10.5-12 K (Fehér et al. 2016) and 10.6 ± 0.1 K (Wu et al. in preparation). Serp S1a has a T_k 10.8 K derived from NH_3 (1,1) (2,2) and 7 K was adopted as T_{ex} (Friesen et al. 2013; Li et al. 2016). The T_{ex} of L492 was derived as 6.4 K from HC_3N and 8.3 K from CO, respectively (Hirota & Yamamoto 2006). L1521B has a T_{ex} of 5.5-6.5 K and its T_K is about 10 K (Hirota et al. 2004; Suzuki et al. 1992). The T_{ex} of C_3S of L1498 ranges from 5.5 to 10 K (Suzuki et al. 1992; Kuiper et al. 1996), and the T_k is 10 K derived from NH_3 emission in this core. The T_d of L1498 is 10 K (Tafalla et al. 2004). The T_{ex} of L1544 is from 5 to 6.5 K (Suzuki et al. 1992) and T_K derived from NH_3 is ~ 10 K, and the T_d of L1544 is also 10 K (Tafalla et al. 2002). In the EMC however, the T_{ex} is 11.5 K derived from HC_3N and T_{rot} is 12.6 K from CH_3CCH , which are similar to the T_{rot} of C_4H_2 (12.3 ± 0.8 K) and CH_3CCH (13.9 K) for L1527 (Sakai et al. 2008). These comparisons show that the gas of the EMC is warmer and closer to thermalization status than those in early starless cores and comparable to that of L1527. These may explain why the carbon-chain molecular emissions in the EMC are similar to those of WCCC sources.

However, there is a fundamental difference in that L1527 contains a protostar which is the heating source of the core material (Goldreich & Kwan 1974; Sakai et al. 2008). For the EMC, there is no protostar inside, only an association with a protostellar object L1489 IRS at one arcminute to the west.

Figure 7 displays the images of 850 μm , 500 μm , and 250 μm continuum emissions as well as molecular line emissions in the L1489 region. One can see that the P point (black triangle), the centers of larger 850 μm continuum core, and the NH_3 core (blue triangle) are close to each other but not overlaid exactly. Such deviation among peaks of different molecular line emission regions are very common in prestellar and stellar cores even in the TMC-1 region (Sánchez-Monge et al. 2014; Keown et al. 2016; Pratap et al. 1997). Cores of other molecular lines such as N_2H^+ $J=1-0$ and CS $J=3-2$ are also coincident with the EMC (Caselli et al. 2002; Zhou et al. 1989). The weaker but larger core in the east of L1489 IRS shown in the SCUBA 850 μm map and the SPIRE 500 μm image covered the EMC entirely.

The L1489 IRS is a Class I source while the one in L1527 is a Class 0 object. The L_{bol} is 3.6-3.8 L_\odot for the L1489 IRS and 1.3-1.9 L_\odot for L1527, respectively (Kristensen et al. 2012; Chen et al. 1995). The T_{bol} of L1527 is 44 K (Kristensen et al. 2012; Chen et al. 1995), while the T_{bol} of the L1489 IRS is 200-283 K and more than five times of that of L1527 on average (Kristensen et al. 2012; Chen et al. 1995). The C_4H emission extends from the center part of the envelope to 5600 AU in L1527. High-energy excitation CCM lines in the EMC are possible to be excited, though L1489 IRS is located at the margins of the EMC since L1489 IRS is has relatively high bolometric luminosity and temperature. Further more, H_2O $1_{1,0}-1_{0,1}$ observed with HIFI on Herschel presents an inverse P-cygni profile in L1527 but a P-Cygni profile in L1489 IRS, indicating that L1489 IRS lacks an outer, cooler gas layer, which is in favor of the heating of its neighboring material.

From Fig. 7 one can see that at each wavelength, the strongest emission is around the IRS. The higher the frequency, the more the contours concentrate at the IRS. The tails of the contours of the 250 μm and 500 μm maps present a trajectory format starting from the IRS, which has not previously been seen in low-mass protostellar cores. These may be the evidence that the EMC is heated by the L1489 IRS. The size of the 250 μm emission region is 169.1 arcsec and T_d from the spectral energy

distribution (SED) fitting based on data of PACS-SPIRE bands is 13.8 K in the whole region.

The heating of L1489 IRS can be more significant considering the possible evolutionary history of the relationship between L1489 IRS and the EMC; they may be neighbors since the birth of L1489 IRS. However, another possibility may be that the IRS has moved away from the EMC center to the cloud margin, or it has dispersed the surrounding gas and has separated itself from the EMC (Harju et al. 1993; Wu et al. 2006). The influences of the L1489 IRS might what gives the EMC its WCCC characteristics.

However, WCCC began from reactions of C^+ and sublimated CH_4 from dust. A precondition is that the temperature needs to be ~ 30 K (Sakai et al. 2009). For L1527, the kinetic temperature is 20–30 K derived from the $c-C_3H_2$ $4_{3,2}-4_{2,1}$ line detected with the Plateau de Bure Interferometer (Sakai et al. 2010a). From the $c-C_3H_2$ and SO lines measured with ALMA with beam sizes $0.8'' \times 0.7''$ and $0.7'' \times 0.5''$ and analyzed with non-LTE large-velocity-gradient code, the kinetic temperatures of the $c-C_3H_2$ emitting region was found as 30 K at 100 AU (Sakai et al. 2014). The kinetic temperatures of L1527 measured from the interferometers are much higher than 13.9 K derived from the CH_3CCH $J=5-4$, $K=1,2$ observed using NRO 45 m telescope with beam size $\sim 20''$. These results present effects of telescope beams. The kinetic temperature of the EMC derived from CH_3CCH $J=5-4$, $K=0,1,2$ detected with the PMO 13.7 m telescope with a beam size of $53''$ is 12.6 ± 1.0 K. The dust temperature fitted from JCMT and Herschel data is 13.8 ± 0.2 K. Both the values of the kinetic and dust temperature are comparable to those of L1527 measured with the NRO 45 m telescope. For the IRS sources, both the L_{bol} and T_{bol} of the L1489 IRS are higher than those of L1527. These comparisons indicate that in a smaller region within the EMC the kinetic temperature may be higher than the current results. Higher-resolution observations are needed to measure the temperature.

In the WCCC source L1527, CCMs of the prestellar phase could survive if the prestellar collapse is faster than that of other star-forming cores (Sakai et al. 2008). The EMC should have an early and a cold phase, like those starless cores shown in Fig. 6. No collapse or infall have been found in the EMC so far. The CCMs detected in the EMC may have survived from its early phase. In particular, the chemical activities of the CCMs seem to be related to their existence in the WCCC phase. Because of the different polarities, the N- and S-bearing species are more active than C_4H and CH_3CCH and more likely to react with their partners. For example, the major loss route of C_4H is through reaction with C^+ (Millar & Freeman 1984): $C_4H + C^+ \rightarrow C_5^+ + H$, which has a rate coefficient of $2.0 \times 10^{-9} \text{ cm}^3$ at 10 K. While the reaction of HC_3N with C^+ : $HC_3N + C^+ \rightarrow C_3HN^+ + C$ has a rate coefficient of $8.7 \times 10^{-9} \text{ cm}^3$ at the same temperature (Leung et al. 1984). However, both species are formed from hydrocarbon ions and the reaction rates are not significantly different from one another (Leung et al. 1984). This suggests that the molecular species with high-energy excitation lines have a higher rate of survival than low-excitation lines, which might be a reason for the emissions of species with high-energy excitation lines in L1527 (Sakai et al. 2008) and the late core EMC. This may also be the reason for the detection of the HC_3N $J=10-9$ line with E_{up} 24.0 K in L1498 (Tafalla et al. 2006).

Besides the high-excitation lines and the N-bearing and S-bearing species discussed above, circular hydrocarbon $c-C_3H_2$ with T_{MB} 1.72 K was also detected in the EMC. The species HC_3N $J=10-9$ with a high upper-level energy of 24.0 K is detected with T_{MB} 0.63 K. Maps of all the detected species

except for C_3S show consistent emission peaks at about 1 arcmin east of the L1489 IRS. These results show that the EMC is an abundant CCM laboratory. Its comparable and contrasting conditions with the WCCC source L1527 and with early cold carbon-chain-producing regions may promote further CCM searches and help to constrain model analyses of CCMs.

5. Summary

Abundant carbon-chain molecules were detected toward the EMC of L1489 IRS, which is identified as a particular carbon-chain-producing region.

1. With the TMRT, HC_3N $J=2-1$, HC_5N $J=6-5$, and HC_7N $J=14-13$, $15-14$, $16-15$ as well as C_3S $J=3-2$ were detected. The T_{MB} of the hyperfine line $J=2-1$ $F=3-2$ of HC_3N is 3.23 K. Five hyperfine lines of HC_3N $J=2-1$ were resolved. Hyperfine components of $F=7-6$, $F=6-5$, and $F=5-4$ of HC_5N $J=6-5$ were resolved for the first time. The T_{MB} of the three rotational lines of HC_7N ranges from 0.25 to 0.32 K. The emission of C_3S $J=3-2$ is the weakest among the detected transitions. Using the PMO telescope, high-energy excitation lines including C_4H $N=9-8$, $J=17/2-15/2$, $19/2-17/2$, CH_3CCH $J=5-4$, $K=2$, and HC_3N $J=10-9$ were detected. The highest upper-level energy is 41.1 K. All the transitions in K_u and 3 mm band are detected for the first time in the EMC of L1489 IRS.

2. Maps of the observed transition lines were also obtained. Emission peaks of our detected lines except C_3S are all located at about $1'$ east of the L1489 IRS, which is consistent with previously detected gas cores and the $850 \mu\text{m}$ continuum east core.

3. The CCM column densities of the EMC were compared with those of TMC-1 together with five carbon-chain-producing regions in early phase (Serp S1a, L492, L1521B, L1498 and L1544) and WCCC source L1527. Results show that the column densities of the species with high-energy excitation lines including CH_3CCH and C_4H in the EMC are close to those of L1527. The C_3S column density of the EMC is slightly lower than that of L1527 but much lower than the five starless cores. The column densities of the N-bearing species are close to those of L1527, and the values of the both sources are at the intermediate level of the starless cores.

4. Similarly to early carbon-chain-producing regions, the EMC is dark, starless, and quiescent. However, the EMC is rather at a late evolutionary stage ($N(NH_3)/N(C_3S)=289$), and is warmer than starless carbon-chain-producing regions. On the other hand, the temperature and thermalization of the EMC are close to those of L1527, though L1527 is a protostellar core. These indicate that the EMC is very special among the carbon-chain-producing regions detected so far.

5. The L1489 IRS has relatively high bolometric luminosity and temperature. The weaker but larger core to the east of L1489 IRS shown in the SCUBA $850 \mu\text{m}$ and the SPIRE $500 \mu\text{m}$ images covered the EMC completely. The tails of the contours of the $250 \mu\text{m}$ and $500 \mu\text{m}$ maps present a trajectory format starting from the IRS. The dust continuum emission area and the morphology of the contours show that the EMC is externally heated by the L1489 IRS.

Acknowledgements. We are grateful to the staff of PMO Qinghai Station and SHAO. We also thank Shanghuo Li, Kai Yang and Bingru Wang for their assistance during the observation period. This project was supported by the grants of National Key R&D Program of China No. 2017YFA0402600, NSFC Nos. 11433008, 11373009, 11373026, 11503035, 11573036, U1331116 and U1631237, and the Top Talents Program of Yunnan Province. This research used the facilities of the Canadian Astronomy Data Centre operated by the the National Research Council of Canada with the support of the Canadian Space Agency.

References

- Askne, J., Hoglund, B., Hjalmarsen, A., & Irvine, W. M. 1984, *A&A*, 130, 311
- Avery, L. W., Broten, N. W., MacLeod, J. M., Oka, T., & Kroto, H. W. 1976, *ApJ*, 205, L173
- Bell, M. B., Feldman, P. A., Travers, M. J., et al. 1997, *ApJ*, 483, L61
- Benedettini, M., Pezzuto, S., Burton, M. G., et al. 2012, *MNRAS*, 419, 238
- Benson, P. J., & Myers, P. C. 1989, *ApJS*, 71, 89
- Brinch, C., Crapsi, A., Hogerheijde, M. R., & Jørgensen, J. K. 2007, *A&A*, 461, 1037
- Broten, N. W., Oka, T., Avery, L. W., MacLeod, J. M., & Kroto, H. W. 1978, *ApJ*, 223, L105
- Bussa, S., & VEGAS Development Team. 2012, in *American Astronomical Society Meeting Abstracts*, Vol. 219, American Astronomical Society Meeting Abstracts #219, 446.10
- Caselli, P., Benson, P. J., Myers, P. C., & Tafalla, M. 2002, *ApJ*, 572, 238
- Chen, H., Myers, P. C., Ladd, E. F., & Wood, D. O. S. 1995, *ApJ*, 445, 377
- Cordiner, M. A., Charnley, S. B., Buckle, J. V., Walsh, C., & Millar, T. J. 2011, *ApJ*, 730, L18
- Evans, II, N. J. 1980, in *IAU Symposium*, Vol. 87, *Interstellar Molecules*, ed. B. H. Andrew, 1–17
- Fehér, O., Tóth, L. V., Ward-Thompson, D., et al. 2016, *A&A*, 590, A75
- Ford, A. B., & Shirley, Y. L. 2011, *ApJ*, 728, 144
- Friesen, R. K., Medeiros, L., Schnee, S., et al. 2013, *MNRAS*, 436, 1513
- Fuller, G. A., & Myers, P. C. 1993, *ApJ*, 418, 273
- Garden, R. P., Hayashi, M., Hasegawa, T., Gatley, I., & Kaifu, N. 1991, *ApJ*, 374, 540
- Goldreich, P., & Kwan, J. 1974, *ApJ*, 189, 441
- Guilloteau, S., & Lucas, R. 2000, in *Astronomical Society of the Pacific Conference Series*, Vol. 217, *Imaging at Radio through Submillimeter Wavelengths*, ed. J. G. Mangum & S. J. E. Radford, 299
- Harju, J., Walmsley, C. M., & Wouterloot, J. G. A. 1993, *A&AS*, 98, 51
- Herbst, E., Smith, D., & Adams, N. G. 1984, *A&A*, 138, L13
- Hirahara, Y., Suzuki, H., Yamamoto, S., et al. 1992, *ApJ*, 394, 539
- Hirota, T., Ito, T., & Yamamoto, S. 2002, *ApJ*, 565, 359
- Hirota, T., Maezawa, H., & Yamamoto, S. 2004, *ApJ*, 617, 399
- Hirota, T., Ohishi, M., & Yamamoto, S. 2009, *ApJ*, 699, 585
- Hirota, T., Sakai, T., Sakai, N., & Yamamoto, S. 2011, *ApJ*, 736, 4
- Hirota, T., & Yamamoto, S. 2006, *ApJ*, 646, 258
- Hogerheijde, M. R., & Sandell, G. 2000, *ApJ*, 534, 880
- Hogerheijde, M. R., van Dishoeck, E. F., Blake, G. A., & van Langevelde, H. J. 1998, *ApJ*, 502, 315
- Irvine, W. M., Ziurys, L. M., Avery, L. W., Matthews, H. E., & Friberg, P. 1988, *Astrophysical Letters and Communications*, 26, 167
- Kaifu, N., Ohishi, M., Kawaguchi, K., et al. 2004, *PASJ*, 56, 69
- Kalenskii, S. V., Slysh, V. I., Goldsmith, P. F., & Johansson, L. E. B. 2004, *ApJ*, 610, 329
- Kauffmann, J., Bertoldi, F., Bourke, T. L., Evans, II, N. J., & Lee, C. W. 2008, *A&A*, 487, 993
- Kawaguchi, K., Kaifu, N., Ohishi, M., et al. 1991, *PASJ*, 43, 607
- Keown, J., Schnee, S., Bourke, T. L., et al. 2016, *ApJ*, 833, 97
- Kristensen, L. E., van Dishoeck, E. F., Bergin, E. A., et al. 2012, *A&A*, 542, A8
- Kroto, H. W., Kirby, C., Walton, D. R. M., et al. 1978, *ApJ*, 219, L133
- Kuiper, T. B. H., Langer, W. D., & Velusamy, T. 1996, *ApJ*, 468, 761
- Lada, C. J. 1985, *ARA&A*, 23, 267
- Leung, C. M., Herbst, E., & Huebner, W. F. 1984, *ApJS*, 56, 231
- Li, J., Shen, Z.-Q., Wang, J., et al. 2016, *ApJ*, 824, 136
- Lovas, F. J. 2004, *Journal of Physical and Chemical Reference Data*, 33, 177
- Mangum, J. G., & Shirley, Y. L. 2015, *PASP*, 127, 266
- Markwick, A. J., Millar, T. J., & Charnley, S. B. 2000, *ApJ*, 535, 256
- Matthews, H. E., Irvine, W. M., Friberg, P., Brown, R. D., & Godfrey, P. D. 1984, *Nature*, 310, 125
- Millar, T. J., & Freeman, A. 1984, *MNRAS*, 207, 405
- Müller, H. S. P., Schlöder, F., Stutzki, J., & Winnewisser, G. 2005, *Journal of Molecular Structure*, 742, 215
- Myers, P. C., Fuller, G. A., Mathieu, R. D., et al. 1987, *ApJ*, 319, 340
- Myers, P. C., Heyer, M., Snell, R. L., & Goldsmith, P. F. 1988, *ApJ*, 324, 907
- Myers, P. C., Linke, R. A., & Benson, P. J. 1983, *ApJ*, 264, 517
- Ohashi, N., Lee, S. W., Wilner, D. J., & Hayashi, M. 1999, *ApJ*, 518, L41
- Olano, C. A., Walmsley, C. M., & Wilson, T. L. 1988, *A&A*, 196, 194
- Ossenkopf, V., & Henning, T. 1994, *A&A*, 291, 943
- Pickett, H. M., Poynter, R. L., Cohen, E. A., et al. 1998, *J. Quant. Spectr. Rad. Transf.*, 60, 883
- Pratap, P., Dickens, J. E., Snell, R. L., et al. 1997, *ApJ*, 486, 862
- Sakai, N., Sakai, T., Hirota, T., Burton, M., & Yamamoto, S. 2009, *ApJ*, 697, 769
- Sakai, N., Sakai, T., Hirota, T., & Yamamoto, S. 2008, *ApJ*, 672, 371
- . 2010a, *ApJ*, 722, 1633
- Sakai, N., Shiino, T., Hirota, T., Sakai, T., & Yamamoto, S. 2010b, *ApJ*, 718, L49
- Sakai, N., Sakai, T., Hirota, T., et al. 2014, *Nature*, 507, 78
- Sánchez-Monge, Á., Beltrán, M. T., Cesaroni, R., et al. 2014, *A&A*, 569, A11
- Saul, M., Tothill, N. F. H., & Purcell, C. R. 2015, *ApJ*, 798, 36
- Shan, W.-Y., Lu, H.-Z., & Shen, S.-Q. 2012, *Phys. Rev. B*, 86, 125303
- Snyder, L. E., Hollis, J. M., Jewell, P. R., Lovas, F. J., & Remijan, A. 2006, *ApJ*, 647, 412
- Suzuki, H., Yamamoto, S., Ohishi, M., et al. 1992, *ApJ*, 392, 551
- Tafalla, M., Myers, P. C., Caselli, P., & Walmsley, C. M. 2004, *A&A*, 416, 191
- Tafalla, M., Myers, P. C., Caselli, P., Walmsley, C. M., & Comito, C. 2002, *ApJ*, 569, 815
- Tafalla, M., Santiago-García, J., Myers, P. C., et al. 2006, *A&A*, 455, 577
- Taniguchi, K., Saito, M., Sridharan, T. K., & Minamidani, T. 2018, *ApJ*, 854, 133
- Turner, B. E. 1971, *ApJ*, 163, L35
- Wang, J. Q., Yu, L. F., Zhao, R. B., et al. 2015, *Acta Astronomica Sinica*, 56, 63
- Wang, Y., Chang, Q., & Wang, H. 2019, *A&A*, 622, A185
- Winnewisser, G., & Walmsley, C. M. 1978, *A&A*, 70, L37
- Wu, Y., Zhang, Q., Chen, H., et al. 2005, *AJ*, 129, 330
- Wu, Y., Zhang, Q., Yu, W., et al. 2006, *A&A*, 450, 607
- Yen, H.-W., Takakuwa, S., Ohashi, N., et al. 2014, *ApJ*, 793, 1
- Zhang, X.-Y., Zhu, Q.-F., Li, J., et al. 2017, *A&A*, 606, A74
- Zhou, S., Wu, Y., Evans, II, N. J., Fuller, G. A., & Myers, P. C. 1989, *ApJ*, 346, 168
- Ziurys, L. M. 2006, *Proceedings of the National Academy of Science*, 103, 12274

Table 1. Observed transitions and telescope parameters

Molecular	Q _{9.375}	Q _{18.75}	Transition	freq.(MHz)	$S_{ij}\mu^2(D^2)$	$E_{low}(K)$	$E_{up}(K)$	FWHM(")	$v_{chan}(m/s)$
HC ₃ N	43.27	86.22	J=2-1 F=1-1	18198.3745	2.311	0.43652	1.30990	52	24
			J=2-1 F=3-2	18196.3104	12.94	0.43667	1.30995	52	24
			J=2-1 F=2-1	18196.2169	6.933	0.43652	1.30980	52	24
			J=2-1 F=1-0	18195.1364	3.081	0.43681	1.31003	52	24
			J=2-1 F=2-2	18194.9195	2.312	0.43667	1.30988	52	24
HC ₅ N	147.1	293.8	J=6-5 F=7-6	15975.9831	43.3	1.91687	2.68359	60	27
			J=6-5 F=6-5	15975.9663	36.4	1.91673	2.68345	60	27
			J=6-5 F=5-4	15975.9336	30.6	1.91687	2.68359	60	27
HC ₇ N	346.7	693.0	J=16-15	18047.9697	325.3	6.49618	7.36235	53	24
			J=15-14	16919.9791	348.5	5.68414	6.49617	56	25
			J=14-13	15791.9870	371.7	4.92634	5.68424	60	27
C ₃ S	68.0	135.5	J=3-2	17342.2564	41.15	0.83234	1.66464	55	25
C ₄ H	165.5	329.7	N=9-8 J=19/2-17/2	85634.00	13.36	16.436	20.546	53	210
			N=9-8 J=17/2-15/2	85672.57	11.94	16.451	20.563	53	210
CH ₃ CCH	34.42	88.27	J=5(0)-4(0)	85457.27	2.81	8.20271	12.30399	53	210
			J=5(1)-4(1)	85455.62	2.70	15.40346	19.50466	53	210
			J=5(2)-4(2)	85450.76	2.36	37.00571	41.10667	53	210
c-C ₃ H ₂	72.4	201.8	J=2(1,2)-1(0,1)	85338.89	52.94	2.3498	6.44539	53	210
HC ₃ N	43.27	86.22	J=10-9	90979.0230	138.6	19.64854	24.01482	53	210

Table 2. Observed and derived parameters

Species	Transitions	V_{LSR}^I (km/s)	T_{MB}^I (mK)	ΔV^I (m/s)	$\int T_{MB} dv^2$ (K m/s)	$N(S)^3$ (10^{12} cm^{-2})
HC ₃ N	J=2-1 F=1-1	6.660(9)	692(110)	177(39)	130(22)	45(4)
	J=2-1 F=3-2	6.650(2)	3230(110)	206(6)	709(18)	
	J=2-1 F=2-1	6.642(4)	2134(111)	164(11)	372(7)	
	J=2-1 F=1-0	6.640(8)	1172(110)	145(18)	172(6)	
	J=2-1 F=2-2	6.640(9)	852(110)	185(30)	167(6)	
HC ₅ N	J=6-5 F=7-6	6.626(5)	628(46)	161(11)	106(5)	9.7(6)
	J=6-5 F=6-5	6.625(5)	629(46)	194(13)	126(5)	
	J=6-5 F=5-4	6.626(8)	427(46)	193(19)	87(5)	
HC ₇ N	J=14-13	6.639(9)	257(30)	184(27)	51(10)	1.4(0.2)
	J=15-14	6.644(9)	318(30)	156(33)	53(10)	
	J=16-15	6.601(7)	252(41)	168(18)	45(4)	
C ₃ S	J=3-2	6.640(9)	161(33)	151(19)	26(3)	0.8(0.1) ⁽⁴⁾
C ₄ H	N=9-8 J=19/2-17/2	6.79(7)	187(35)	520(120)	122(24)	45(8)
	N=9-8 J=17/2-15/2	6.78(3)	266(35)	535(87)	105(15)	
CH ₃ CCH	J=5(0)-4(0)	6.74(4)	220(9)	359(155)	91(4)	
	J=5(1)-4(1)	6.72(3)	170(9)	350(40)	83(8)	20(3)
	J=5(2)-4(2)	6.72(3)	42(8)	310(40)	12(8)	
c-C ₃ H ₂	2(1,2)-1(0,1)	6.77(4)	1720(40)	563(15)	671(16)	5.5(0.1)
HC ₃ N	J=10-9	6.70(2)	629(45)	416(45)	254(15)	3.4(0.3)

⁽¹⁾ The uncertainties of V_{LSR} , T_{MB} and ΔV are obtained from Gaussian fitting.

⁽²⁾ The uncertainties of $\int T_{MB} dv$ are calculated from error transfer formula.

⁽³⁾ Column densities of species are adopted as average values calculated from different hyperfine lines weighted by T_{MB}/σ , assuming all are optical thin with an identical excitation temperature, except that of HC₃N based on HC₃N $J = 2 - 1$ whose optical depths are derived from HFS fitting and that of CH₃CCH whose column density is adopted as the value given by rotation diagram. Uncertainties of column densities are calculated from error transfer formula, including the error introduced from the uncertainty of excitation temperature.

⁽⁴⁾ C₃S parameters at O point are listed.

Table 3. Dust parameters

Source	S ₇₀ Jy	S ₁₆₀ Jy	S ₂₅₀ Jy	S ₃₅₀ Jy	S ₅₀₀ Jy	Size ₂₅₀ arcsec	T _d K	N _{H₂} 10^{22} cm^{-2}
L1489	38.07	84.69	102.86	75.58	38.22	169.07	13.8(0.2)	1.0(0.1)

(The 850 μm flux (5.78 Jy) is combined for the SED of L1489, which is from (Hogerheijde & Sandell 2000).)

Table 4. Temperatures

T _{ex} (HC ₃ N) (K)	T _{rot} (CH ₃ CCH) (K)	T _d (K)	T _d (inner-outer) (K)
11.5(1.0)	12.6(1.0)	13.8(0.2)	11.7-12.4

(The T_d(inner-outer) is model fitted from the SCUBA 850 μm map of L1489 (Ford & Shirley 2011).)

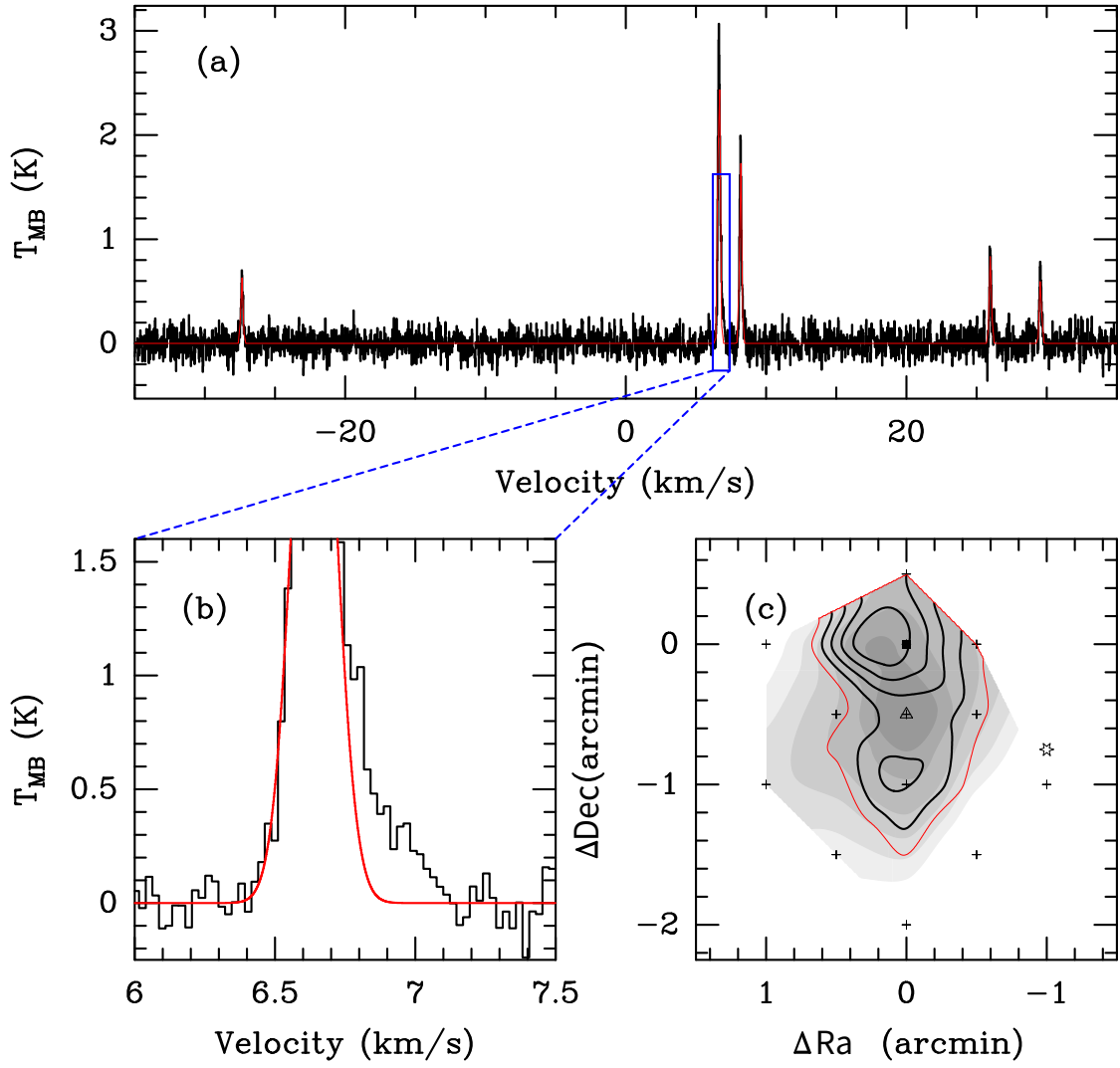


Fig. 1. (a): HC_3N J=2-1, F=3-2 spectrum of the peak position. Red lines show the Gaussian fitting. (b): Zoom-in of panel (a) showing line wing of HC_3N J=2-1, F=3-2. (c): Background is integrated map of HC_3N J=2-1, F=3-2. Black contours represent integration of red wing (6.75 km/s – 7.08 km/s) of HC_3N J=2-1, F=3-2 stepped from 60 to 90 % by 10 % of maximum value 0.14 K km/s. The red contour denotes 3σ level (0.06 K km/s) of HC_3N wing integration. The filled black square represents O point, and the black triangle represents P point (see text). The IRS is shown by the hexagonal star (Yen et al. 2014). Small black crosses show sampled points of K_u band observation.

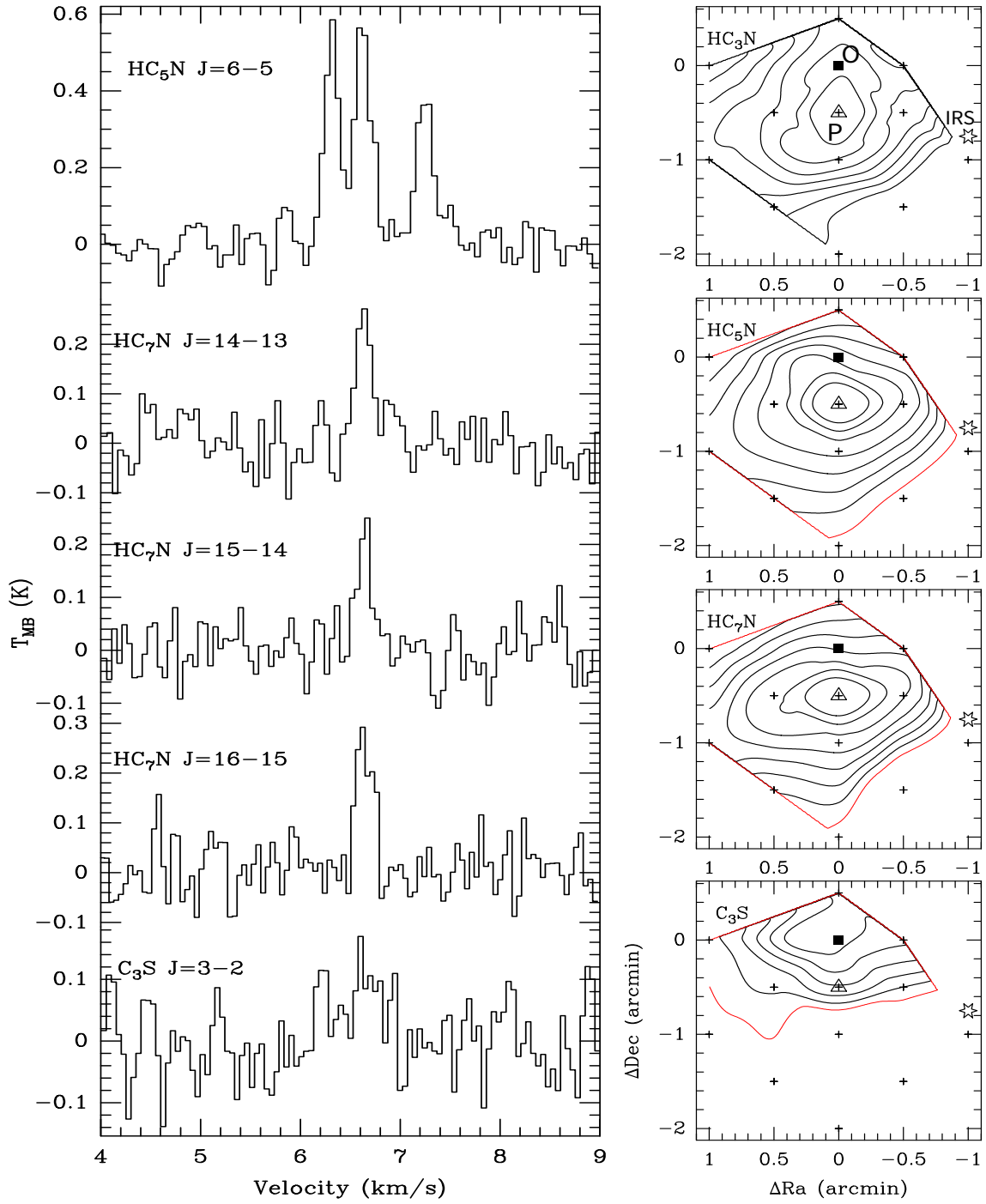


Fig. 2. Emissions of $\text{HC}_3\text{N } J=2-1$, $\text{HC}_5\text{N } J=6-5$, and $\text{HC}_7\text{N } J=14-13$ as well as the $\text{C}_3\text{S } J=3-2$ in K_u band. Left: Spectral lines at the P point. The emission of $\text{HC}_3\text{N } J=2-1$, $F=3-2$ is shown in Fig. 1(a). Right: Intensity contours from 50% to 90% in steps of 10% of the peak value (see Table 2) for $\text{HC}_3\text{N } J=2-1$, $F=3-2$, $\text{HC}_5\text{N } J=6-5$, and $\text{HC}_7\text{N } J=14-13$ as well as $\text{C}_3\text{S } J=3-2$. Red contours represent 3σ of integrated emissions. The symbols are the same as those in Fig. 1(c)

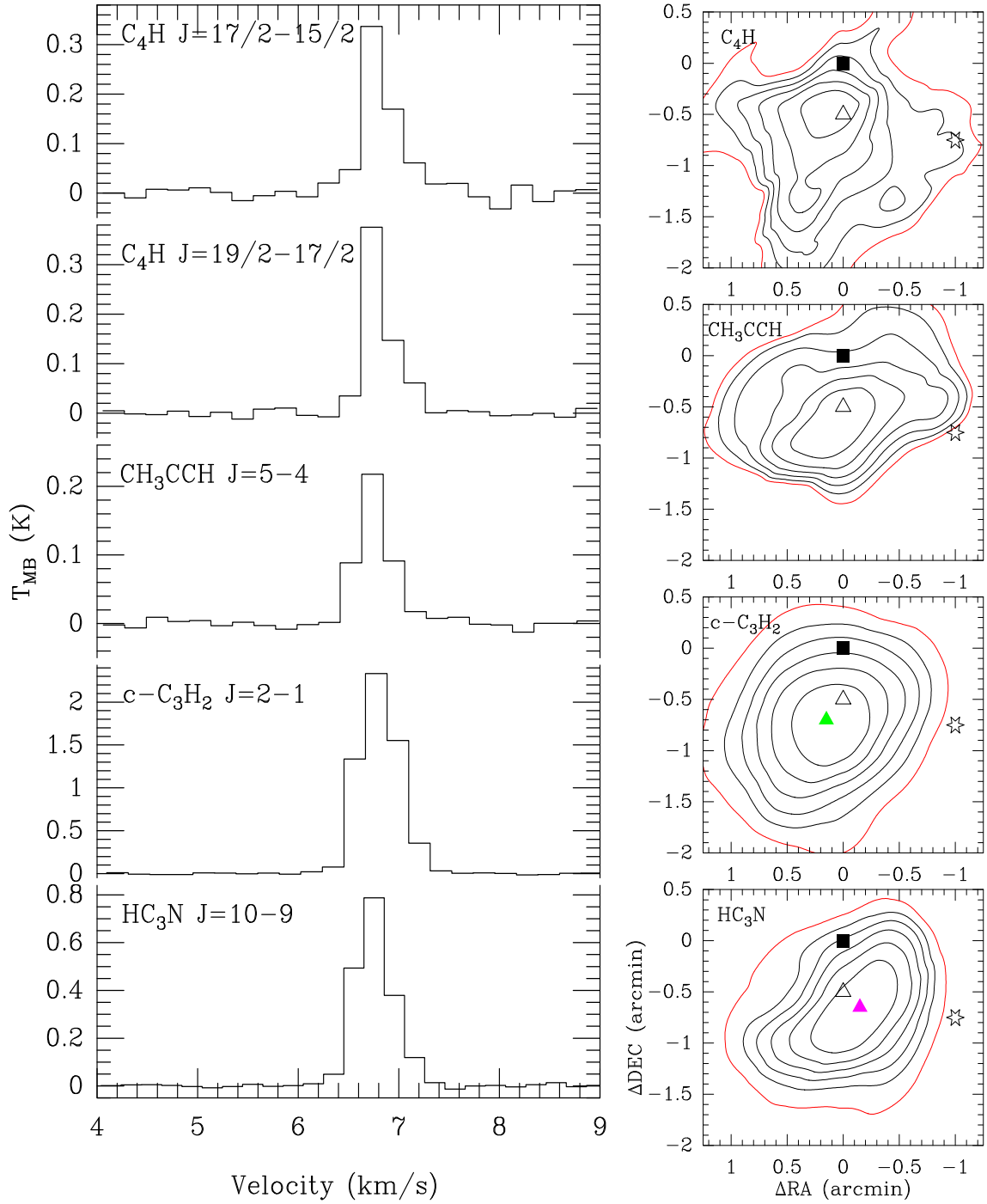


Fig. 3. Emissions of the transitions in the 3 mm band. Left: Spectral lines of the P point. Right: Emission intensity contours from 50% to 90% in steps of 10% of the peak value (see Table 2). C_4H $N=9-8$, $J=19/2-17/2$ and C_4H $N=9-8$, $J=17/2-15/2$ are summed up and shown as C_4H intensity contours. Red contours represent 3σ of integrated emissions. The symbols are the same as those in Fig. 1(c). The green and pink filled triangles represent peak position of $\text{c-C}_3\text{H}_2$ $J=2-1$ and HC_3N $J=10-9$ emission, respectively.

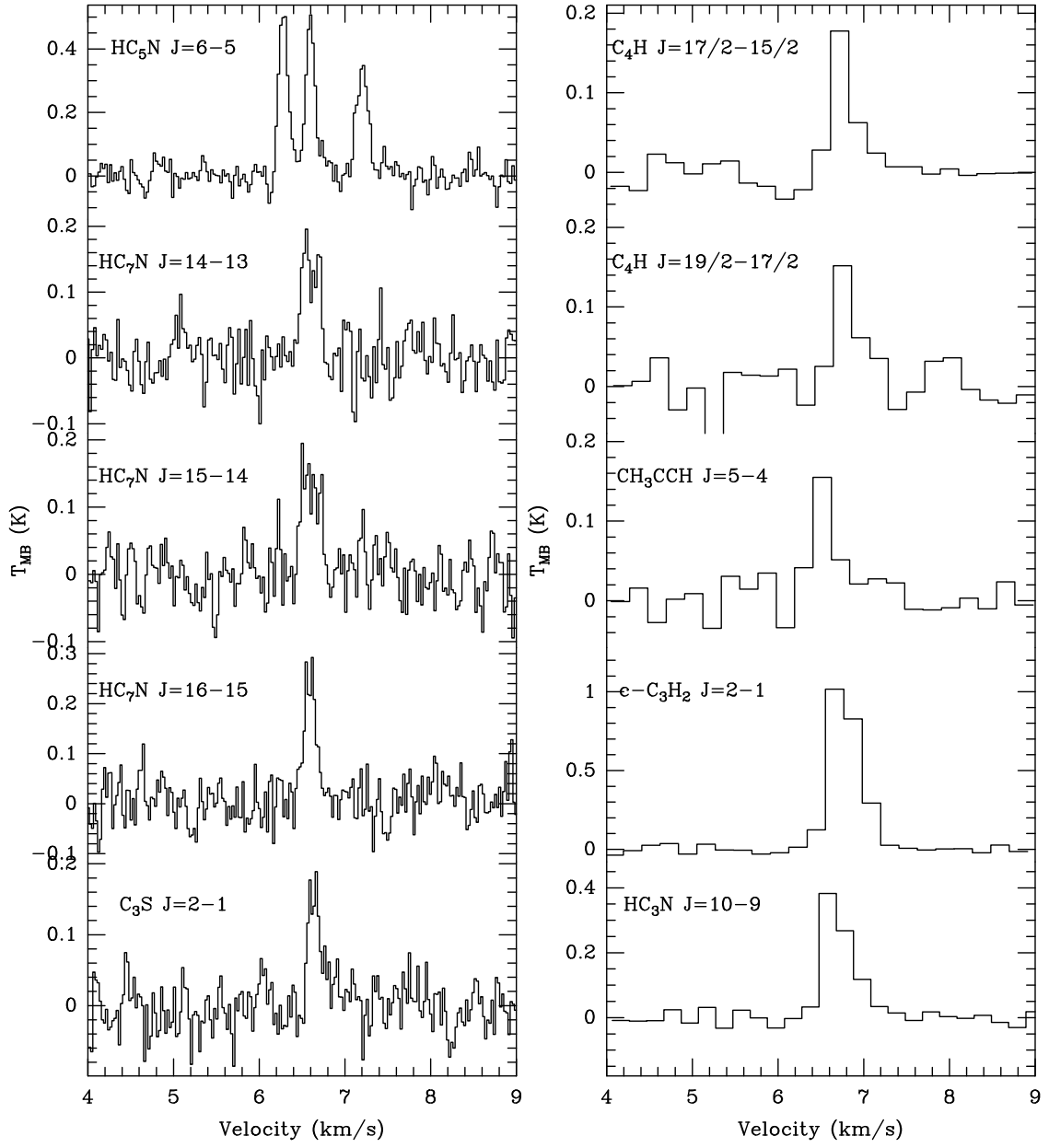


Fig. 4. Spectra at O position. Left: Spectra at K_u band. Right: Spectra at the 3 mm band detected with the 13.7 m telescope of PMO.

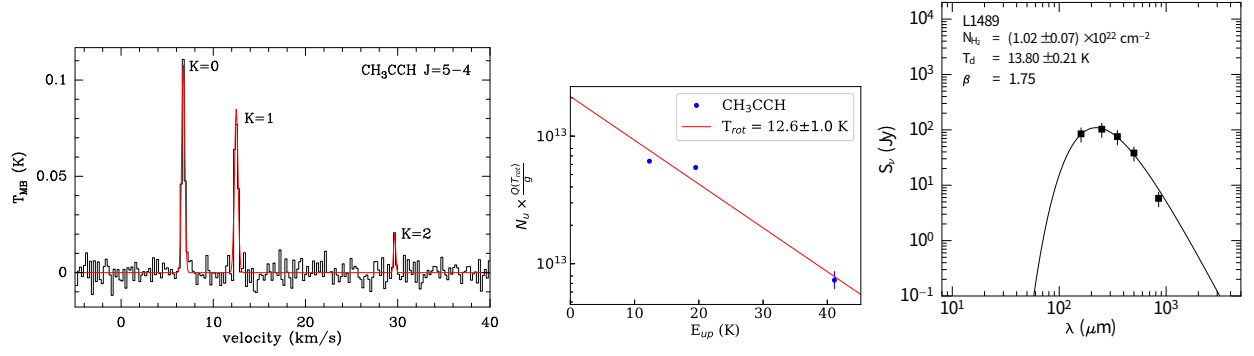


Fig. 5. Left: Spectra of CH_3CCH $J=5-4$, $K=0,1,2$. Middle: Rotation temperature diagram of CH_3CCH . Right: SED of the L1489 IRS from the PACS $160 \mu\text{m}$ and SPIRE wavelengths of Herschel as well as SCUBA $850 \mu\text{m}$. The filled squares represent the input fluxes. The line shows the best fitting of the gray-body model.

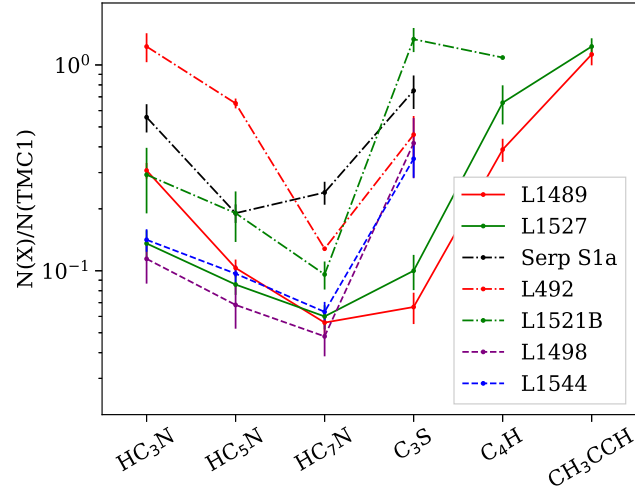


Fig. 6. Comparison between the CCM column densities of L1489 EMC and typical CCM rich sources, normalized by the values of TMC-1 (Kaifu et al. 2004; Suzuki et al. 1992). The source names are denoted in the lower-right corner with different colors, including starless cores Serpens South 1a (Serp S1a; Li et al. 2016), L492 (Hirota & Yamamoto 2006; Hirota et al. 2009), L1521B (Suzuki et al. 1992; Hirota et al. 2004), L1498 (Suzuki et al. 1992; Kuiper et al. 1996) and L1544 (Suzuki et al. 1992) as well as WCCC source L1527 (Sakai et al. 2008). The HC_7N column density of L1544 is derived from that of HC_5N assuming the ratio of $\text{HC}_{2n+1}/\text{HC}_{2n+3}$ ($n=1,2$) is constant (Suzuki et al. 1992). The $N(\text{C}_3\text{S})$ of L1527 is deduced from column densities of C_2S and the ratio of the $\text{C}_3\text{S}/\text{C}_2\text{S}$ (Sakai et al. 2008; Suzuki et al. 1992).

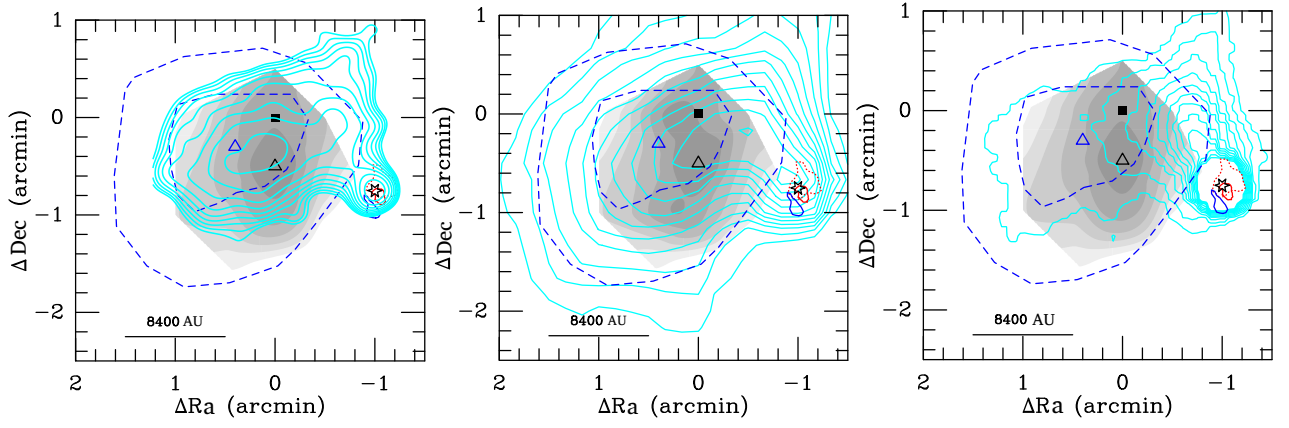


Fig. 7. Left: The HC_3N core (gray-scale) and the NH_3 (1,1) core (blue dashed lines, quoted from Myers et al. (1988)) are overlaid on the JCMT SCUBA $850\ \mu\text{m}$ continuum data from JCMT proposal ID M97AN16 (Hogerheijde & Sandell 2000) (cyan contours, evenly stepped from 0.075 to 0.75 Jy/beam in log-scale). The gray and blue triangles denote the peaks of the EMC (P point) and NH_3 , respectively. The IRS is also marked on the map (hexagonal star). The blue and red wings of the CO (3-2) outflow (blue solid and red dotted lines, quoted from Hogerheijde et al. (1998)) and the medium infalling lobe (red solid line, quoted from Yen et al. (2014)) were also overlaid on the figure. Middle: As in left panel except cyan contours representing Herschel SPIRE $500\ \mu\text{m}$ continuum map, from 1.5 Jy/beam to 5 Jy/beam stepped by 0.3 Jy/beam. Fluxes around the IRS are centrally peaked but higher level contours are not shown. Right: As in left panel except cyan contours representing Herschel SPIRE $250\ \mu\text{m}$ continuum contours, from 1.5 Jy/beam to 5 Jy/beam stepped by 0.3 Jy/beam. Fluxes around the IRS are centrally peaked but higher level contours are not shown.